World Academy of Science, Engineering and Technology
International Journal of Biomedical and Biological Engineering
Vol:16, No:10, 2022

Optical Verification of an Ophthalmological Examination Apparatus Employing the Electroretinogram Function on Fundus-Related Perimetry

Naoto Suzuki

Open Science Index, Biomedical and Biological Engineering Vol:16, No:10, 2022 publications.waset.org/10012731.pdf

***Abstract*—**Japanese are affected by the most common causes of eyesight loss such as glaucoma, diabetic retinopathy, pigmentary retinal degeneration, and age-related macular degeneration. We developed an ophthalmological examination apparatus with a fundus camera, precisely fundus-related perimetry (microperimetry), and electroretinogram (ERG) functions to diagnose a variety of diseases that cause eyesight loss. The experimental apparatus was constructed with the same optical system as a fundus camera. The microperimetry optical system was calculated and added to the experimental apparatus using the German company Optenso's optical engineering software (OpTaliX-LT 10.8). We also added an Edmund infrared camera (EO-0413), a lens with a 25 mm focal length, a 45° cold mirror, a 12 V/50 W halogen lamp, and an 8-inch monitor. We made the artificial eye of a plane-convex lens, a black spacer, and a hemispherical cup. The hemispherical cup had a small section of the paper at the bottom. The artificial eye was photographed five times using the experimental apparatus. The software was created to display the examination target on the monitor and save examination data using C++Builder 10.2. The retinal fundus was displayed on the monitor at a length and width of 1 mm and a resolution of 70.4 ± 4.1 and 74.7 ± 6.8 pixels, respectively. The microperimetry and ERG functions were successfully added to the experimental ophthalmological apparatus. A moving machine was developed to measure the artificial eye's movement. The artificial eye's rear part was painted black and white in the central area. It was rotated 10 degrees from one side to the other. The movement was captured five times as motion videos. Three static images were extracted from one of the motion videos captured. The images display the artificial eye facing the center, right, and left directions. The three images were processed using Scilab 6.1.0 and Image Processing and Computer Vision Toolbox 4.1.2, including trimming, binarization, making a window, deleting peripheral area, and morphological operations. To calculate the artificial eye's fundus center, we added a gravity method to the program to calculate the gravity position of connected components. From the three images, the image processing could calculate the center position.

***Keywords*—**Ophthalmological examination apparatus, microperimetry, electroretinogram, eye movement.

I. Introduction

GLAUCOMA, diabetic retinopathy, pigmentary retinal degeneration, and age-related macular degeneration are the most common causes of eyesight loss. Fig. 1 depicts the prevalence of the major diseases that can lead to eyesight loss in Japan [1]. Since the overall prevalence of the major diseases was 62.5%, we developed an experimental ophthalmological apparatus for diagnosing them.

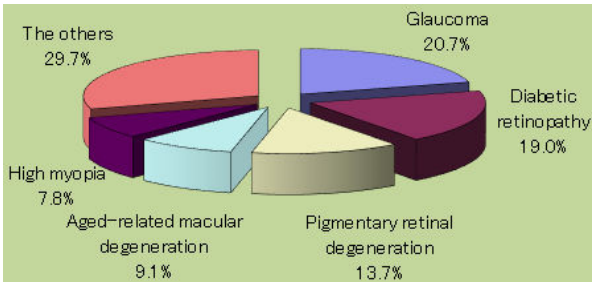

Fig. 1 The prevalence of the major diseases that can lead to eyesight loss [1]

Next, we described the development of an experimental apparatus for detecting diabetic retinopathy. In Japan, the total number of diabetics, including potential patients, was only 16.2 million in 2005, and approximately 3,000 people lose their vision each year as a result of this disease [2]. In contrast, the number of diabetics in the United States has increased from 16 million to 30 million since 1999 [3]. On the other hand, we used the ERG and precisely fundus-related perimetry (microperimetry) to review the pathogenic mechanisms of cryptogenic diseases, such as macular dystrophy, acute zonal occult outer retinopathy (AZOOR), and multiple evanescent white dot syndromes (MEWDS) [4]. Macular dystrophy is a broad term that refers to functional disorders of the macula lutea such as Stargardt's disease, occult macular dystrophy, vitelliform macular dystrophy, and cone-rod dystrophy [5]-[8]. The b-wave of the ERG was selectively diminished in patients with macular dystrophy [9]. AZOOR causes an acute functional disorder in the retinal outer layer [10]. The a-wave and b-wave amplitudes of ERGs were characteristically reduced by 30 Hz flicker responses in patients with AZOOR [11]. MEWDS primarily affects young women, causing acute visual loss and a narrowed visual field for mainly young women [12]. ERG a-wave amplitude was reduced in patients with MEWDS [13].

For the diagnosis of early diabetic retinopathy, we constructed an experimental apparatus with the same optical system as a fundus camera. Finally, we added microperimetry and ERG functions to the experimental apparatus. In our experimental setup, we replaced the color camera with an

N. Suzuki is with National Institute of Technology, Numazu College, Numazu, Shizuoka, Japan (phone: 81-55-926-5789; fax: 81-55-926-5780; e-mail: n-suzuki@numazu-ct.ac.jp)

Open Science Index, Biomedical and Biological Engineering Vol:16, No:10, 2022 publications.waset.org/10012731.pdf

infrared camera and the strobe with a halogen lamp, as shown in Fig. 2. Furthermore, we installed an optical system that included a monitor and a cold mirror. The optical system includes microperimetry and ERG functions. The microperimetry test displays the target to be examined on the monitor. A multifocal hexagonal stimulus array is also displayed on the monitor during the electroretinography test. Hence, we developed an experimental ophthalmological apparatus that combines the functions of a fundus camera, microperimetry, and electroretinography to diagnose a variety of diseases that can lead to eyesight loss. On the other hand, we have to measure the movement of an artificial eye. We developed a moving machine and painted the artificial eye's fundus. To measure the artificial eye's movement, we used labeling of binary images and a gravity method of connected components. We used connected-component labeling to detect connected regions in the binary images [14], [15]. When integrated into not only an image recognition system but also a human-computer interaction interface, connected-component labeling can operate on various types of information [16]. On the other hand, a graph is created from input data and consists of vertices and connecting edges. The vertices contain information needed for comparison. However, the edges indicate connected neighbors. Then, after labelling the vertices based on connectivity and relative values, the algorithm traverses the graph. The connectivity is determined by the medium, and image graphs can have four or eight connected neighborhoods [17]. The binary data are iterated using a two-pass algorithm [18], and the algorithm is known as the Hoshen–Kopelman algorithm.

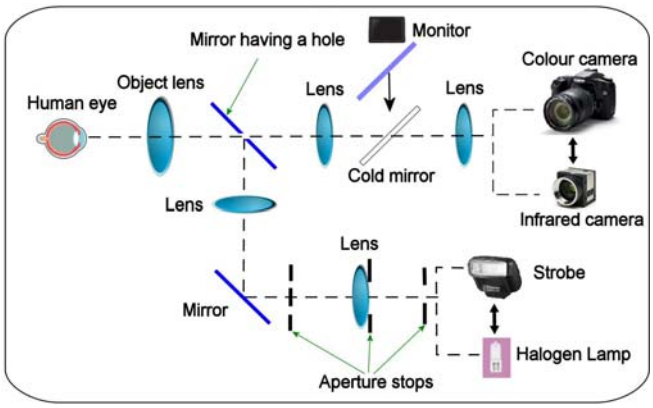

Fig. 2 Experimental apparatus including the microperimetry and ERG functions

II. Methods

A. Experimental Apparatus and Artificial Eyes

The experimental apparatus, as shown in Fig. 3, consists of an illumination optical system and a photographic optical system separated by a mirror having a hole with a 4 mm diameter.

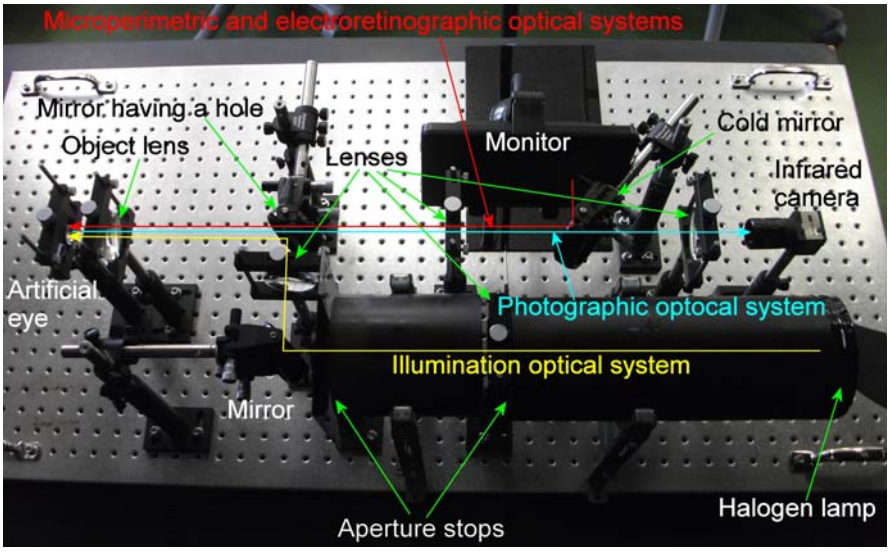

Fig. 3 An experimental apparatus

The apparatus consists of an Edmund infrared camera EO-0413, a lens with a 25 mm focal length, a 12V/50W halogen lamp, an object lens with a 50 mm focal length, four double-convex lenses with a 100 mm focal length, two aperture stops, a mirror, a 45° cold mirror, a Century Corporation's 8-inch monitor LCD-8000V, and an artificial eye. Furthermore, the experimental apparatus includes microperimetric and electroretinographic optical systems separated by a cold mirror. The 8-inch monitor displays the microperimetry examination targets and the ERG 's multifocal hexagonal stimulus array. Fig. 4 depicts our artificial eye, which resembles the Gullstrand eye model [19]. As shown in Fig. 4 (a), the artificial eye consists of a plane-convex lens, a black spacer, and a hemispherical cup. It was 20 mm in diameter. The plane-convex lens has a 4.6-mm center thickness and a 17.4-mm back focal length. The hemispherical cup is made of polyethylene terephthalate and

measures 20 mm in diameter and 0.5 mm in thickness. Therefore, the distance between the plane-convex lens surface and the fundus was 22.5 mm. A small section of the paper was stuck to the bottom of the hemispherical cup, as shown in Fig. 4 (b).

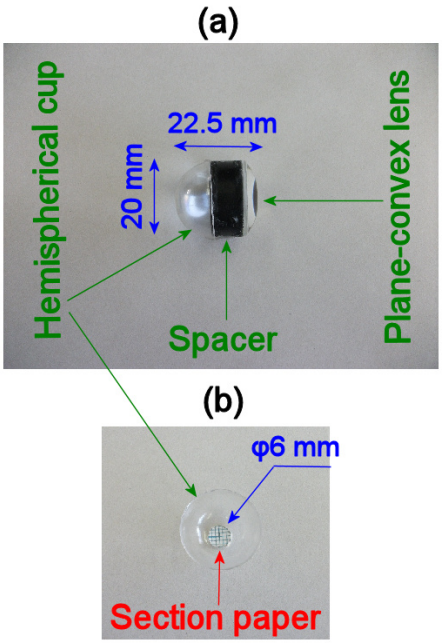

Fig. 4 An artificial eye

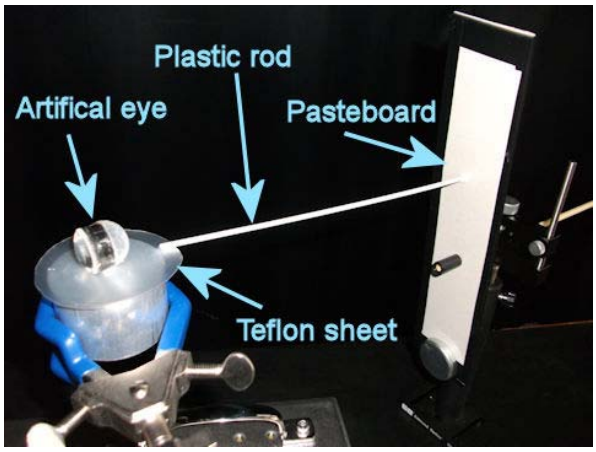

Fig. 5 A Prototype model of the moving machine

B. Measuring the Resolution of the Artificial Eye's Fundus

The artificial eye was photographed five times with the experimental apparatus. We measured four lengths in each image. To obtain the ratio of the length on the monitor to the length on the artificial fundus, we counted the pixels of the retinal fundus on the monitor at a length and width of 1 mm.

C. Developing Microperimetry and Electroretinography Software

We developed microperimetry and electroretinography software using C++ Builder 10.2. Using the microperimetry software, a doctor can select a point on a fundus image. The software can display the examination targets in the same location on the monitor and save the examination data. Additionally, the software can perform static perimetry. The electroretinography software can then display a 37-element the multifocal hexagonal stimulus array.

D. Measuring the Artificial Eye's Movement

As shown in Fig. 5, we developed a moving machine to measure the artificial eye's movement.

The moving machine was made up of a pasteboard, a plastic rod, a Teflon sheet, and an artificial eye. The machine employed the pendulum principle, as shown in Fig. 6.

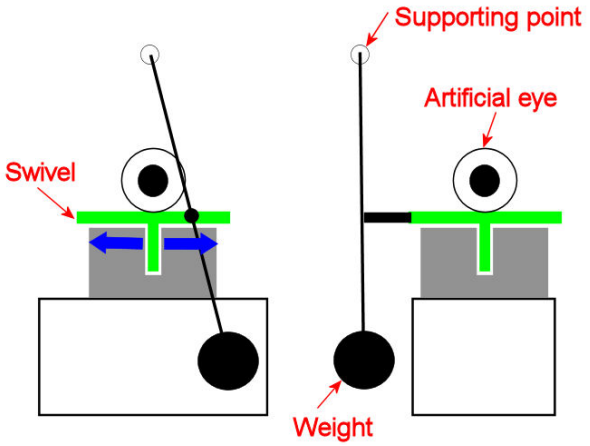

Fig. 6 The moving machine principle

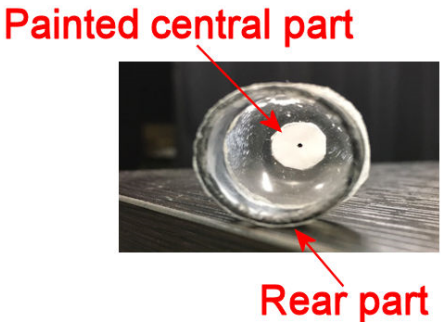

Fig. 7 The artificial eye's rear part is painted on the central area

The artificial eye was mounted on a swivel to transmit the pendulum's periodic motion. The swivel was constructed from a Teflon sheet and an aluminum column. The pendulum consisted of the pasteboard and a weight. The plastic rod was used to transmit the periodic motion. Then, we made a rear part of the artificial eye and painted black and white on the central area, as shown in Fig. 7. We swapped the section paper-covered rear part for the newly painted rear part. The moving machine caused the artificial eye to rotate 10 degrees from side to side. The movement was captured five times as motion videos using the experimental apparatus. Furthermore, we extracted three static images from one of the motion videos captured. The three static images depict an artificial eye facing three directions: center, right, and left. The three images were processed using the cross-platform numerical computational software, Scilab

Open Science Index, Biomedical and Biological Engineering Vol:16, No:10, 2022 publications.waset.org/10012731.pdf

Open Science Index, Biomedical and Biological Engineering Vol:16, No:10, 2022 publications.waset.org/10012731.pdf

6.1.0, and Image Processing and Computer Vision (IPCV) Toolbox 4.1.2 with five processes: trimming, binarization, making a window, deleting peripheral area, and morphological operation (Fig. 8) [20], [21].

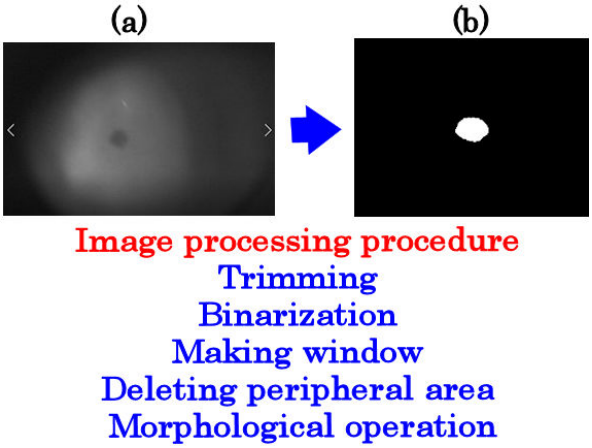

Fig. 8 An image processing procedure

"Trimming" is the process of cropping images to a rectangle. "Binarization" is the process of converting images to binary images. A few noises were present in the binarized image's peripheral area. "Making a window" means creating a window. The term "deleting peripheral area" refers to removing noises from the peripheral area using the window. That is, we eliminate the noises outside the window. A "morphological operation" is the creation of a structural element for a morphological operation. The function constructs and returns the structural element, which can then be passed to any morphology filter. We can also create an arbitrary mask and use it as a structuring element. In addition, we include a program in the image processing that uses a gravity method to calculate the center of the artificial eye's fundus. In the binarization image, brightness 0 shows a black pixel, but brightness 1 also shows a white pixel. There will be a component connected with many white pixels near the center of the fundus. The program calculates the gravity position of the connected component.

III. Results

A. Resolution of the Artificial Eye's Fundus

The image extracted from the fundus image of the artificial eye is shown in Fig. 9. We used a Century LCD-8000V monitor with a resolution of 800 × 600 pixels. The experimental apparatus was able to display the retinal fundus on the monitor at a length and width of 1 mm and a resolution of 70.4 ± 4.1 and 74.7 ± 6.8 pixels, respectively. Therefore, we could extrapolate the ratio of the length of the monitor to the length of the artificial fundus.

B. Microperimetry Test

Fig. 10 depicts the situation in which the position for the examination target is selected in the microperimetric examination test. After a doctor clicked a manifestation position on the monitor with a mouse, the software could measure the x and y coordinates of the position.

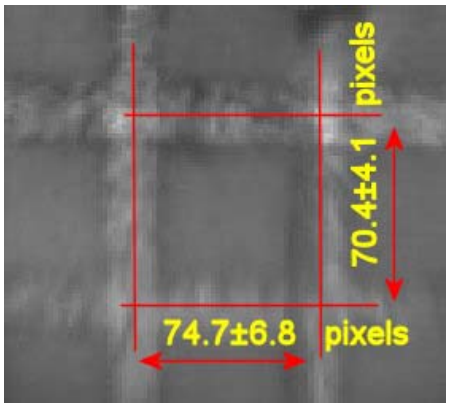

Fig. 9 The image extracted from the artificial eye's fundus image

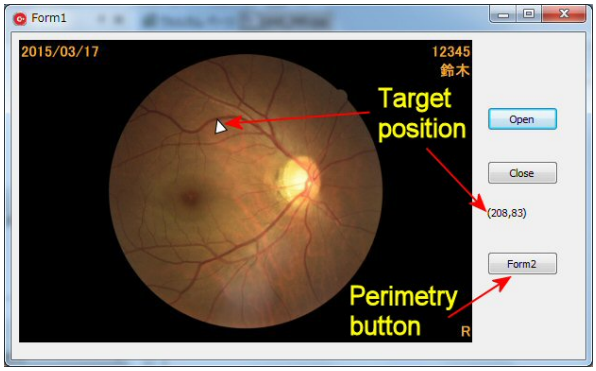

Fig. 10 The software for the microperimetric examination test

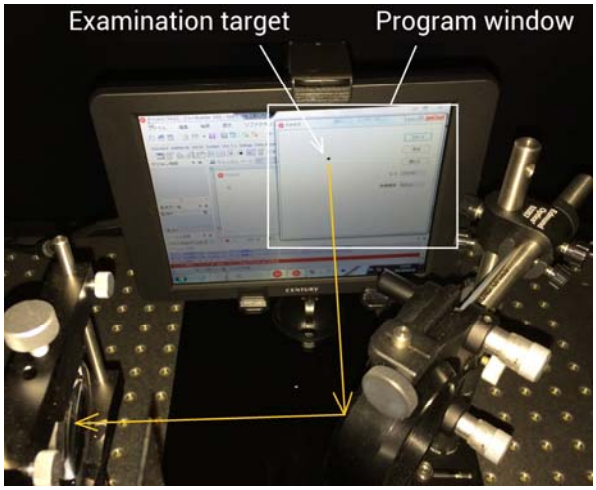

Fig. 11 The monitor in the microperimetric examination test

Fig. 11 depicts the situation in which the examination target is displayed in the microperimetric examination test. After the doctor clicked the perimetry button, the examination target could be displayed on the same x and y coordinates in the perimetric window. However, the background luminance was low (31.5 apostilbs), and the examination target was very small. We needed to take a photo of the microperimetry test to clearly show the examination target (Fig. 11). In fact, we used a

Open Science Index, Biomedical and Biological Engineering Vol:16, No:10, 2022 publications.waset.org/10012731.pdf

background lighter than 31.5 apostilbs and an examination target darker than the real luminance.

C. Electroretinography Test

The electroretinography test is depicted in Fig. 12. We used a 37-element multifocal hexagonal stimulus array in the software. The software could display the multifocal hexagonal stimulus array by inverting the white and black elements at regular intervals. In collaboration with the microperimetry software, the center of the multifocal hexagonal stimulus array can be adjusted to the same position as the examination target of the microperimetry.

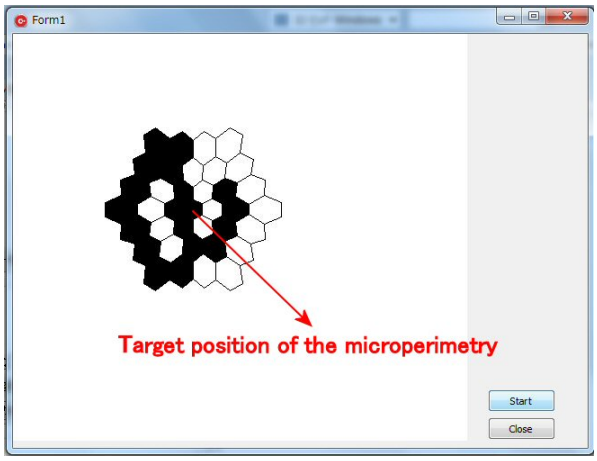

Fig. 12 An electroretinography test

D. Measurement of the Artificial Eye's Movement

We captured the five motion videos using the moving machine. From a single-motion video, three static images were extracted. The static images depicted the artificial eye facing the center (Fig. 13), the right (Fig. 14), and the left (Fig. 15) directions.

Using Scilab 6.1.0 and the IPCV Toolbox 4.1.2, the three images were processed (Figs. 13-15). The original images had a resolution of 530 x 341 pixels. The images were trimmed by the program, and their resolution has decreased to 250 x 250 pixels. The images were then binarized by the program with a threshold value specified in the range from 0 to 1, regardless of the input image class. We set the binarization threshold value to 0.62. Fig. 16 (a) depicts the binarized image of Fig. 13. Because the peripheral area contains a lot of noise, we created a window to remove it, as shown in Fig. 16 (a). All of the noise outside the window was completely eliminated, as shown in Fig. 16 (b). However, a little noise was left on the right side. We then performed a morphological operation. There are three types of structural elements: rect; ellipse; and cross. The ellipse was chosen as the structural element. The number of rows and columns are both natural numbers. We chose 15 for both the row and the column. The morphological operation has three parameters: structure type; number of rows; and number of columns. The remaining noise was removed as shown in Fig. 16 (c). Furthermore, we used the gravity method to calculate the center of the artificial eye's fundus. We were able to calculate the gravity position of the component that was connected with many white pixels near the fundus center. In the three images (Figs. 17-19), the analysis results were depicted as a red cross. Fig. 17 depicts the artificial eye facing the center. The center positions (x and y) were determined as 126.29 and 128.12, respectively.

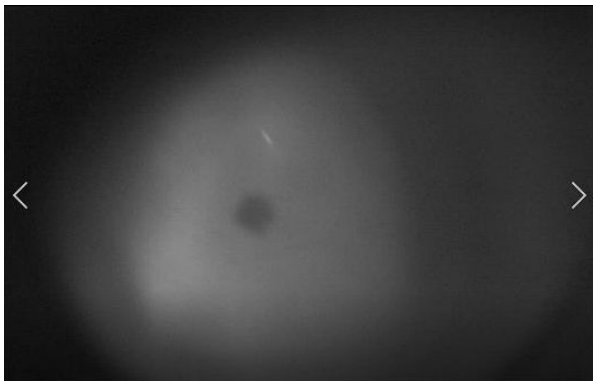

Fig. 13 An artificial eye facing the center direction

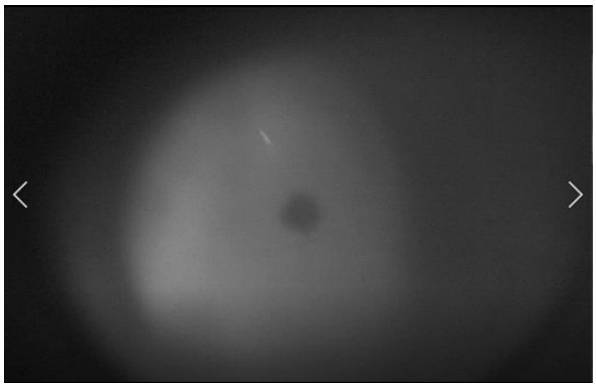

Fig. 14 An artificial eye facing the right direction

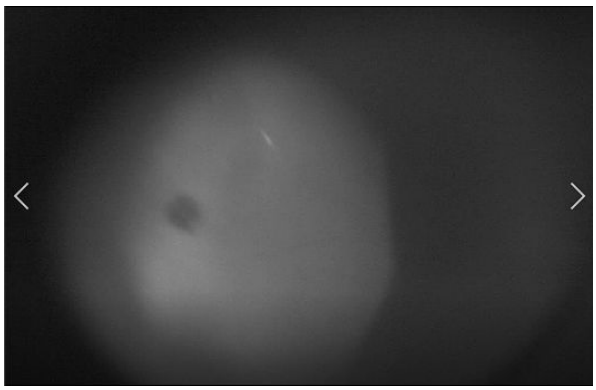

Fig. 15 An artificial eye facing the left direction

Fig. 18 depicts the artificial eye facing the right direction. The center positions (x and y) were determined as 172.34 and 128.23, respectively.

Fig. 19 depicts the artificial eye facing the left direction. The center positions (x and y) were determined as 60.69 and 126.02, respectively.

Open Science Index, Biomedical and Biological Engineering Vol:16, No:10, 2022 publications.waset.org/10012731.pdf

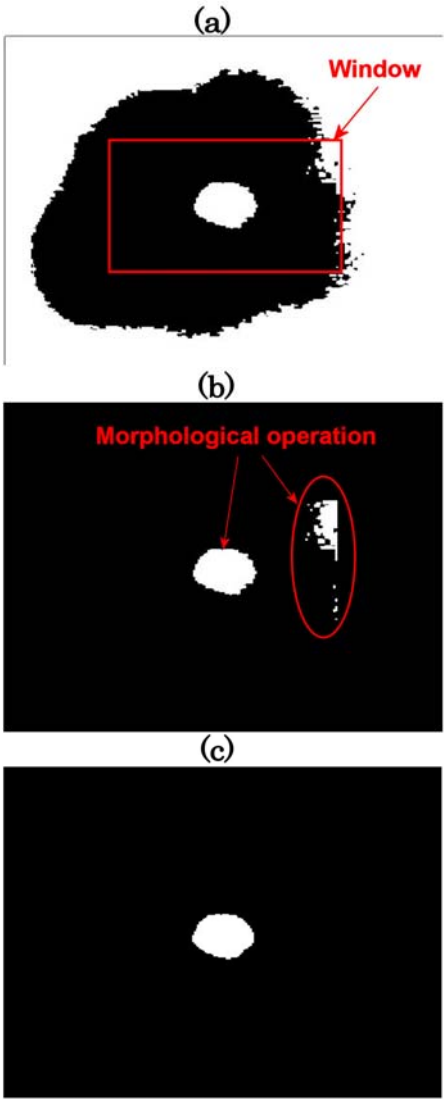

Fig. 16 Making a window and deleting the peripheral area

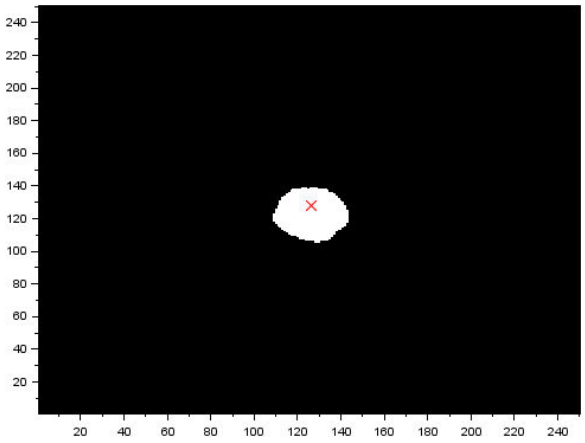

Fig. 17 Calculation of the fundus center position facing the center direction

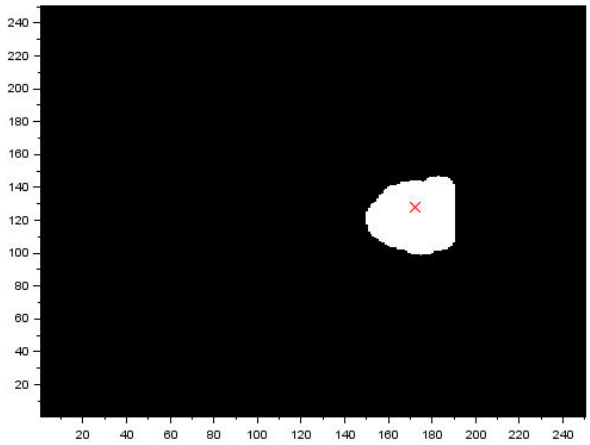

Fig. 18 Calculation of the fundus center position facing the right direction

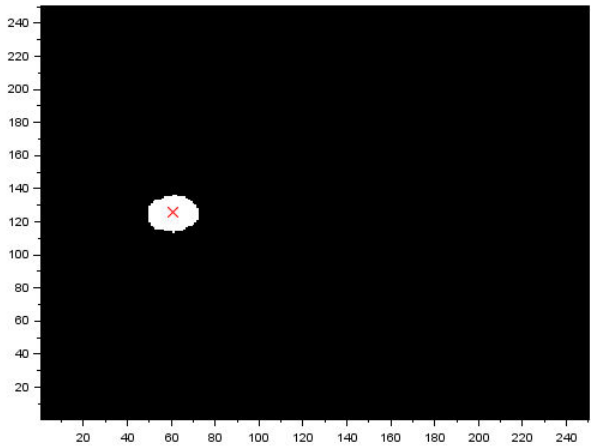

Fig. 19 Calculation of the fundus center position facing the left direction

IV. Conclusion

We developed the ophthalmological examination apparatus, to which microperimetry and electroretinography functions were added. The ophthalmological apparatus was optically verified by measuring the resolution and movement of the artificial eye. The moving artificial eye center was measured using the five image processing and gravity methods.

Acknowledgment

The National Institute of Technology, Numazu College, funded this research. We are thankful to all those who helped and contributed to this study.

References

[1] K. Nakae, F. Kogure et al., "Recent epidemiological of the visual loss in Japan", Journal of Health and Welfare Statistics 38(7), 1991, pp13-22.
[2] T. Tsuchiya, "Measure Against Lifestyle Related Disease," JMAJ, Vol.49 No.3, 2006, pp.132-134.
[3] Z.T. Bloomgarden, "American Diabetes Association Annual Meeting, 1999, Diabetes and obesity," Diabetes Care, Vol.23, No.1, 2000, pp.118-124.
[4] N. Suzuki, "Development of Moving Multifocal Electroretinogram with a Precise Perimetry Apparatus", International Journal of Biomedical and

Biological Engineering, Vol.13, No.11, 2019, pp465-469.
[5] M. Michaelides, D.M. Hunt, A.T. Moore, "The genetics of inherited macular dystrophies", J Med Genet, Vol.40 No.9, 2003, pp641-650.
[6] N Lois, G.E. Holder, C Bunce, F.W. Fitzke, A.C. Bird, "Phenotypic subtypes of Stargardt macular dystrophy-fundus flavimaculatus", Arch Ophthalmol, Vol.119 No.3, 2001, pp359-369.
[7] Y Miyake, K Ichikawa, Y Shiose, Y Kawase, "Hereditary Macular Dystrophy without Visible Fundus Abnormality", Am J Ophthalmol, Vol.108 No.3, 1989, pp292-299.
[8] C.J. Boon, B.J. Klevering, B.P. Leroy, C.B. Hoyng, J.E.E. Keunena, A.I. den Hollander, "The spectrum of ocular phenotypes caused by mutations in the BEST1 gene", Prog Retin Eye Res, Vol.28 No.3, 2009, pp187-205.
[9] J.J. Kanski, B. Bowling, "Macular Dystrophies" in Clinical Ophthalmology: Systematic Approach, 7th Edition, Amsterdam: Elsevier-Health Sciences Division, 2011, pp665-670.
[10] J.D. Gass, "Acute zonal occult outer retinopathy. Donders Lecture: The Netherlands Ophthalmological Society, Maastricht, Holland, June 19, 1992", J Clin Neuroophthalmol, No.13, 1993, pp79-97.
[11] J.J. Kanski, B. Bowling, "Acute zonal occult outer retinopathy" in Clinical Ophthalmology: Systematic Approach, 7th Edition, Amsterdam: Elsevier-Health Sciences Division, 2011, pp594-595.
[12] L.M. Jampol, P.A. Pugh et al, " Multiple evanescent white dot syndrome, 1. Clinical findings", Arch Ophthalmol, No.102, 1984, pp671-674.
[13] J.J. Kanski, B. Bowling, "Multiple evanescent white dot syndrome" in Clinical Ophthalmology: Systematic Approach, 7th Edition, Amsterdam Elsevier-Health Sciences Division, 2011, pp588-589.
[14] H. Samet, M. Tamminen, "Efficient Component Labeling of Images of Arbitrary Dimension Represented by Linear Bintrees", IEEE Transactions on Pattern Analysis and Machine Intelligence Vol.10, No.4, 1988, pp579-586.
[15] M.B. Dillencourt, H. Samet, M. Tamminen, "A general approach to connected-component labeling for arbitrary image representations", Journal of the ACM, Vol.39, No.2, 1992, pp253-280.
[16] K. Wu, W. Koegler, J. Chen, A. Shoshani, "Using bitmap index for interactive exploration of large datasets", 15th International Conference on Scientific and Statistical Database Management, Cambridge, MA, 2003, pp1-10.
[17] R. Fisher, S. Perkins, A. Walker, E. Wolfart, "Connected Component Labeling", 2003, Retrieved 15 July 2022.
[18] L.G. Shapiro, G.C. Stockman, " Computer Vision", Prentice Hall, 2001, pp.69–73.
[19] A. Gullstrand, “How I found the mechanism of intracapsular accommodation”, Nobel Lectures, Physiology or Medicine 1901, pp414-431.
[20] C. Gomez (Editor), "Engineering and Scientific Computing with Scilab", Birkhauser, 1999.
[21] P. Roux, "Scilab from theory to practice: I. Fundamentals", Scilab Enterprise, 2016.

Naoto Suzuki graduated from Chuo University in 1994; he also received a Master of Engineering from Chuo University in 1996. He was a Ph.D. candidate in the Graduate School of Engineering, The University of Tokyo, and earned the necessary credits, but he left the doctoral course in 2000. His research focused on developing an ophthalmologic device while working with a medical equipment maker and received a Ph.D. from Chiba University in 2007. He was an Assistant Professor at Hiroshima International University from 2009 to 2013. He has been an Associate Professor at the National Institute of Technology, Numazu College since 2014.

Open Science Index, Biomedical and Biological Engineering Vol:16, No:10, 2022 publications.waset.org/10012731.pdf